PERGAMON

Journal of Structural Geology 23 (2001) 1531–1547

JOURNAL OF STRUCTURAL GEOLOGY

www.elsevier.com/locate/jstrugeo

Fracture characterization of chalk in uniaxial and triaxial tests by rock mechanics, fractographic and electromagnetic radiation methods

Dov Bahat[a,*], Avinoam Rabinovitch[b], Vladimir Frid[a]

[a]*Department of Geological and Environmental Science and The Deichmann Rock Mechanics Laboratory of the Negev, Ben-Gurion University of the Negev, Beer Sheva 84105, Israel*

[b]*Physics Department and The Deichmann Rock Mechanics Laboratory of the Negev, Ben-Gurion University of the Negev, Beer Sheva 84105, Israel*

Received 27 July 2000; revised 25 January 2001; accepted 30 January 2001

Abstract

This study relates to fracture characterization of chalk in uniaxial and triaxial tests by combined application of rock mechanic, fractographic and electromagnetic radiation (EMR) methods. We found high strength results ($\sigma_1 - \sigma_3$) that ranged from 37.7 to 52.6 MPa. We identified several 'key surface morphologies' that were distinct from each other, and expanded on their characterization according to tensile and shear categories. Tensile features include plumes (or striae) and stairs. Shear features include a sugary texture, ridges and grooves and steps. Fracture surfaces induced by tension and shear show distinct morphologies. Longitudinal splitting domains can occur continuously on an axial, tensile plane or adjacent parallel planes. On the other hand, shear failure into meso-fractures (up to about 10 cm in length) is a process that combines a series of distinct domains on separate surfaces that slightly differ in curvature and orientation, and are inclined to the sample axis. Four fracture sequences that initiated either in tensile or in shear surfaces were distinguished in the failed samples. Results obtained by rock mechanics and by EMR methods are well correlated for microcracks and for meso-fractures and may vary over five orders of magnitude in size, and this correlation is partially supported by fractography. In particular, a very good linear relationship was obtained between the ratio of the time interval to reach EMR pulse envelope maximum and the pulse frequency (T'/ω) and the largest fractures formed. Extrapolating this result enabled us to calculate fracture sizes when the value of T'/ω was known. © 2001 Elsevier Science Ltd. All rights reserved.

Keywords: Uniaxial; Triaxial; Tensile; Shear; Fractography; Electromagnetic radiation; Domains; Sub-domains

1. Introduction

Rock mechanics of chalk are of great importance in planning and carrying out engineering, hydrological, environmental and oil production in chalk provinces throughout the world (e.g. Burland, 1990). Fractography has turned out to be a useful tool in studying joints cutting chalks in outcrop scale (Bahat, 1991) but was not really explored in laboratory scales. The inducement of electromagnetic radiation (EMR) by brittle fracture was successfully applied to determine crack dimensions (e.g. Rabinovitch et al., 1998). We aim in this study to experimentally characterize the failure of chalk under both uniaxial and triaxial loadings, by combining together rock mechanics, EMR and fractographic methods, with the expectation of widening the horizon of each of these individual methods. The new observations, when compared with previous experimental results, will enable a fresh evaluation of certain geological problems.

1.1. Rock mechanical tests

Two experimental techniques are used to test fracture in rock. They differ by the form of the initial sample: some investigators use 'virgin' samples that are tested without introducing any discontinuities to the rock (e.g. Jaeger and Cook, 1979), while others prefer 'pre-cracked' samples into which two initial flaws are introduced (e.g. Bobet, 2000). The failure of virgin rock samples better reveals the behavior of the rock in nature and the influence of sample boundaries on fracture initiation. On the other hand, the artificial pre-cracked samples help to investigate the growth, interaction and coalescence of fractures that grow from the early flaws. In this study, we concentrate on virgin samples, but compare our results with those obtained from samples tested by both techniques. Scott and Nielsen (1991) compared results obtained by triaxial tests on sandsone

---

* Corresponding author. Tel.: +972-7-6472-623; fax: +972-7-6472-997.
E-mail address: bahat@bgumail.bgu.ac.il (D. Bahat).

0191-8141/01/$ - see front matter
PII: S0191-8141(01)00018-9

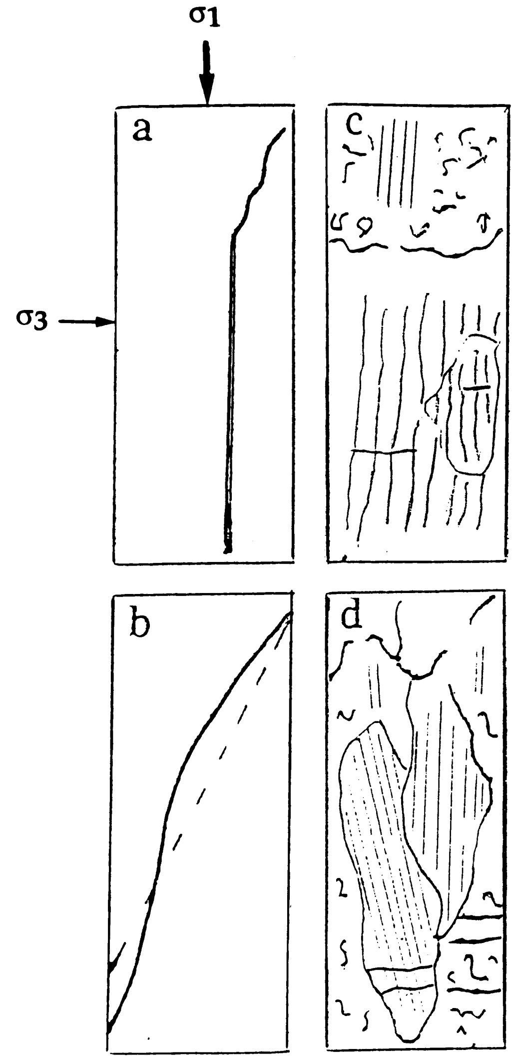

Fig. 1. Various types of brittle fracture developed experimentally in rocks. (a) Longitudinal splitting by uniaxial stress in continuation of initial conic fracture induced by boundary effects at the end of the sample. (b) Shear fracture by triaxial stress, showing formal straight conjugate cut (dashed line) and actual curved fracture. (c, d) Parallel sections in the Beer Sheva chalk. (c) Derived by a uniaxial test, showing a shear surface, above, separated by a boundary from a tensile surface subdivided into domains below it. (d) Curved profile of meso-fracture formed by a triaxial test, showing adjacent domains marked by ridges and grooves at different orientations.

samples of the above two types and pointed out similarities and differences in their fracture parameters.

Fracture properties of rock are often characterized in relation to stress-strain curves (Jaeger and Cook, 1979). These tests commonly use rocks that are cut into cylinders with a ratio of length to diameter, which ranges from two to three, where the stresses in the central portion of the specimen are affected only slightly by contact with the endcup. Specimens with smaller ratios are more significantly affected by the endcup, while for specimens with larger ratios, reduced strength results may be expected (Jaeger and Cook, 1979, p. 145).

Uniaxial test results show that tensile longitudinal splitting often forms sub-parallel to the cylindrical axis and to the maximum principal stress, σ_1, while shear fractures usually result from triaxial loading and are inclined at a small fracture angle, α (in the range 20–30°) relative to the σ_1 direction (Fig. 1a–d). The literature on uniaxial and triaxial tests is vast, and here we only touch on a few key papers relevant to the present investigation and expand on this subject in later parts of this paper (Section 4).

As yet there is no satisfactory explanation of the process leading to longitudinal splitting. Holzhausen and Johnson (1979) argue that generally, without buckling, axial splitting at $\alpha = 0$ cannot occur by tension. If, however, buckling of the rock occurs, splitting may be initiated within the sample, and may propagate axially by tension to both ends of the cylinder. Holzhausen and Johnson (1979) suggest that sub-axial splitting at $\alpha > 0$ by shear has not been observed by earlier researchers in triaxial tests because the lateral confinement has reduced the effective shear stress along the sub-axial microcracks to zero. Nemat-Nasser and Horii (1982) suggest that relative frictional sliding of the faces of pre-existing cracks at various angles that deviate from axiality may produce at their tips tension cracks that curve into ‘wing cracks’ and grow stably parallel to σ_1.

Shen et al. (1995) and Bobet and Einstein (1998) investigated the various modes of crack propagation in prismatic specimens of gypsum under uniaxial and biaxial compression. The specimens were pre-fractured by two flaws that were inclined to the axial compression. They examined the fractography of the cracks as they propagated and distinguished between tensile cracks (smooth surfaces) and shear cracks (rough surfaces). The shear cracks generally propagated co-planarly with the pre-fractured flaws, i.e. they were inclined to the axial compression, whereas the tensile cracks that propagated in an out-of-plane manner from the pre-fractured flaws, assumed a close to axial orientation, mostly as wing cracks. Characteristically shear cracks preceded the tensile ones, and often initial shear cracks continued to propagate as tensile cracks. In experiments with larger angles between the initial flaws, the role of tensile cracks was greater. At high deviations, coalescence between the flaws was accomplished solely by tensile wing cracks. Finally, the wing cracks disappeared in experiments that were conducted at high confining stresses.

Investigators have suggested various models concerning propagation geometries of early microcracks in relation to the sample shape, and also different interaction mechanisms that would ultimately lead to failure under triaxial loadings. We compare below our results from chalk failure by uniaxial and triaxial loadings with previous observations obtained by uniaxial, biaxial and triaxial tests performed on various materials. It is a common practice to evaluate the results of fracture tests on sections normal to the strikes of these fractures (e.g. Griggs and Handin, 1960; Hallbauer et al., 1973) (Fig. 1a and b), which we term the ‘normal section’, while the section that contains the strike and dip

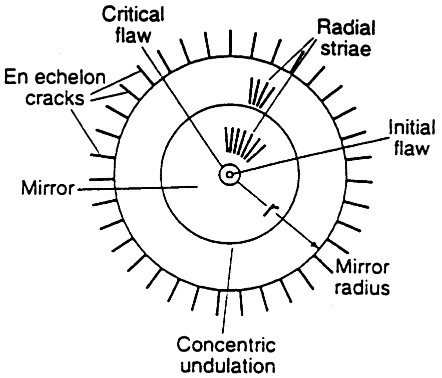

Fig. 2. Schematic representation of various fractographic elements on an 'ideal' fracture surface (after Bahat et al. (1999)).

of the fractures (Fig. 1c and d) is termed the 'parallel section'.

1.2. Fractography

Fractography analyzes fracture surface morphology (or fracture markings) and related features, and probes their causes and mechanisms in engineering materials. Fractographic applications are described in most modern textbooks on structural geology (e.g. Twiss and Moores, 1992; Ghosh, 1993; Davis and Reynolds, 1996), and a detailed introduction of this subject is not considered necessary here. A summary of the numerous fractographic features appearing on an 'ideal' joint surface are given in Fig. 2. On real fracture surfaces, however, only 2–3 elements usually appear. Fractography has been shown to be a competent tool in the investigation of jointing and related tectonophysical problems in chalks, due to the fine grain size of these rocks (e.g. Bahat, 1991). The features of particular interest in the present study are striae (plumes), undulations and en échelon segmentation.

1.3. Electromagnetic radiation in rocks fracture

Fracture propagation is a phenomenon that involves the breaking of atomic bonds and the inducement of atomic oscillations, which lead to the emission of electrons, positive ions and electromagnetic radiation. The latter is deemed to be due to charge acceleration and is known to consist of both an electric field component and a magnetic field component that are perpendicular to each other and to their direction of propagation (transversal waves, similar to water waves excited by a stone) (e.g. Nettel, 1995). The EMR emanating from fractured rocks has a frequency range of between 20 KHz and 20 MHz, i.e. within the radio-wave band of the EMR spectrum.

Stepanov first observed EMR in fractured samples of rock salt (KCl) in 1933 (Urusovskaja, 1969). The phenomenon was measured for fracture in various materials, including metals and alloys (Jagasivamani and Iyer, 1988), single crystals (Nitsan, 1977; Khatiashvili, 1984), ice (Fifolt et al., 1993) and rocks (Nitsan, 1977; Warwick et al., 1982; Ogawa et al., 1985; Cress et al., 1987; Yamada et al., 1989; O'Keefe and Thiel, 1995). In nature, EMR occurs during mine rockburst (Khatiashvili, 1984; Nesbitt and Austin, 1988; Frid, 1997a,b) and also appears as a precursor to earthquakes, some hours or even days before the earthquake event (Mogi, 1985; Yoshino and Tomizawa, 1989; Bella et al., 1992). Hence, EMR is associated with fracture at a variety of scales and is connected to various applications. Several models on an atomic scale have been suggested to explain the EMR phenomenon, but these models were only qualitative, and all efforts to use EMR for quantitative earthquake prediction have hitherto met with no success (King, 1983; Rabinovitch et al., 1998).

In our previous work, it was shown that EMR appears as individual pulses (see below) or as pulse clusters, and we have recently developed a semi empirical equation for the description of the temporal shape of an individual EMR pulse. We have particularly considered the theoretical and experimental relationships between EMR and crack dimensions (Rabinovitch et al., 1996, 1998, 1999; Frid et al., 2000). We have also correlated EMR activity with various mechanical characteristics and investigated the amplitude-frequency relations of pulses (Rabinovitch et al., 1999).

An EMR pulse can be characterized by the following general relationship (Rabinovitch et al., 1998) (Fig. 3):

$$A = A_0 \sin[\omega(t - t_0)]\,[1 - \exp(-(t - t_0)/\tau)], \qquad t < T$$

$$\begin{aligned} A = {} & A_0 \sin[\omega(t - t_0)] \exp(-(t - T)/\tau) \\ & \times [1 - \exp(-(T - t_0)/\tau)], \qquad t \geq T \end{aligned} \tag{1}$$

where t is time, A is the time dependent pulse height, t_0 is the time from the origin up to the pulse beginning and T is the time from the origin up to the EMR pulse envelope maximum. Thus, $T' = T - t_0$ is the time interval to reach pulse envelope maximum, τ is the rise-and-fall times (RFT), which turn out to be the same, A_0 is the pulse amplitude and ω is its frequency. In a recent study (Rabinovitch et al., 2000) we derived the expression $S = kT'/\omega$, where S is the crack area and k is a proportionality constant (see below). In the present study, we correlate variations of the T'/ω parameter obtained by EMR to changes of crack sizes in chalk obtained by fractography.

2. Methods of investigation

2.1. Sample preparation

We used chalk from the Horsha Formation (Middle Eocene), sampled in the Beer Sheva syncline, Israel. The density of all investigated samples was 2.16 ± 0.01 g/cm^3. In order to ensure maximum uniformity of our specimen, we drilled out our cylindrical samples at the same orientation normal to a large vertical, straight joint (smooth fracture

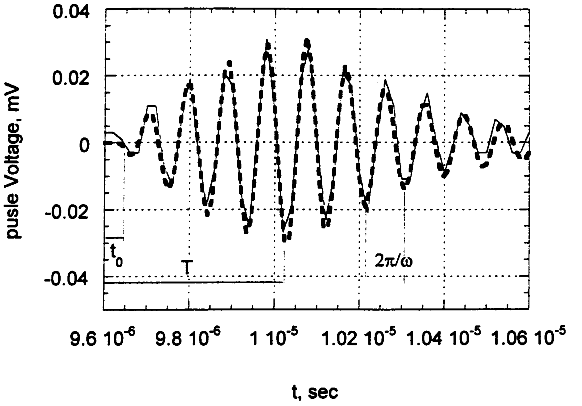

Fig. 3. An experimental EMR pulse and its numerical fit. For this pulse, t_0 is 9.63 μs, T is 10.07 μs. Hence, T' $(T - t_0)$ is 0.44 μs. The frequency ω is 6. 76×10^7 s^{-1}. Therefore, T'/ω is 6.51×10^{-15}.

surface), at exactly the same height of a given layer, in an outcrop remote from other joints or faults. A total of 30 samples of standard size were gathered: cylinders 100 mm long and 52 mm in diameter. The same drying procedure was followed for all samples. This involved heating to 110°C for 24 h, and then immediately removing the sample to a desiccator, in order to avoid any water reabsorption. Most samples were maintained there until mounted into the press machine for the fracture test. Sample 9, on the other hand, went through the standard heat treatment but was not kept in the desiccator (and presumably adsorbed moisture). The strength result for this sample was considerably smaller than for the other ones (Table 1).

2.2. Rock mechanics and EMR investigation

The experimental assemblage was described in detail in our previous paper (Rabinovitch et al., 1998) and is only briefly mentioned here (Fig. 4). We used a TerraTeck rigid press (stiffness 5×10^9 N/m), which was combined with a closed-loop servo control for monitoring axial piston displacements. The load was measured with a sensitive load cell, while the confining pressure was constantly controlled by a clock-type sensor. The cantilever set (consisting of axial and lateral detectors) enabled us to measure sample strains in three orthogonal directions parallel to the three principal stresses. We measured the EMR inside a thick-wall steel pressure vessel in order to render the background noise level negligible. A magnetic one-loop antenna, 3 cm in diameter, was used for the detection of the EMR. We monitored EMR activity in the frequency band from 10 kHz to 50 MHz with an overall sensitivity of up to 1 μV. All samples were jacketed in plastic jackets and the contacts of their ends with the endcups were carefully closed. Samples were axially loaded up to about 70 MPa, at a strain rate of 1×10^{-5} s^{-1}, and in the triaxial tests the lateral load was changed from 0.8 to 15 MPa. All registered EMR pulses were digitized, recorded and analyzed in real

Table 1
Fractographic results of shear/tensile fracture areas under different stress conditions at failure

Sample number	Shear area (SRA) mm^2	Tension area (TNA) mm^2	Total area (TA) mm^2	Shear area/ tension area (SRA/TNA)	Number of cracks	σ_3 MPa	σ_1 MPa	$\sigma_1 - \sigma_3$ MPa
27	4825	1	4825	4825.00	1	5	44	39
17	4487	117	4604	38.35	2	15	65.1	50.1
16	3970	312.5	4282.5	12.70	2	10	54.2	44.2
18	7050	787	7837	8.96	5	3	48.4	45.4
22	4440	700	5140	6.34	3	2	45.8	43.8
26	6357	1762	8119	3.61	5	5	43.5	38.5
19	6700	2025	8725	3.31	4	0.8	46	45.2
21	5443	1662	7105	3.27	3	2	48.8	46.8
11	8351	2610	10961	3.20	12	1	47.6	46.6
15	3762	1457.5	5219.5	2.58	3	5	56.2	51.2
14	6563	2762	9325	2.38	4	1	39.7	38.7
20	6750	2882	9632	2.34	8	0.85	47.5	46.65
25	5549	2576	8125	2.15	7	2	48.7	46.7
23	5687	3450	9137	1.65	4	2	47.9	45.9
12	4850	3400	8250	1.43	4	1	40.7	39.7
6	7598	6417	14015	1.18	11	0	52.6	52.6
1	6557	5795	12352	1.13	7	0	46.9	46.9
10	4692	6112	10804	0.77	3	0	37.7	37.7
2	6082	9160	15242	0.66	16	0	47.6	47.6
4	6296	10768	17064	0.58	18	0	50.4	50.4
8	4327	8078	12405	0.54	12	0	41.9	41.9
3	3299.5	6430	9729.5	0.51	10	0	45.2	45.2
7	4034	7933	11967	0.51	8	0	46.2	46.2
5	5132	10906	16038	0.47	13	0	51.5	51.5
9	3523	3649	7172	1.04	2	0	25.3	25.3

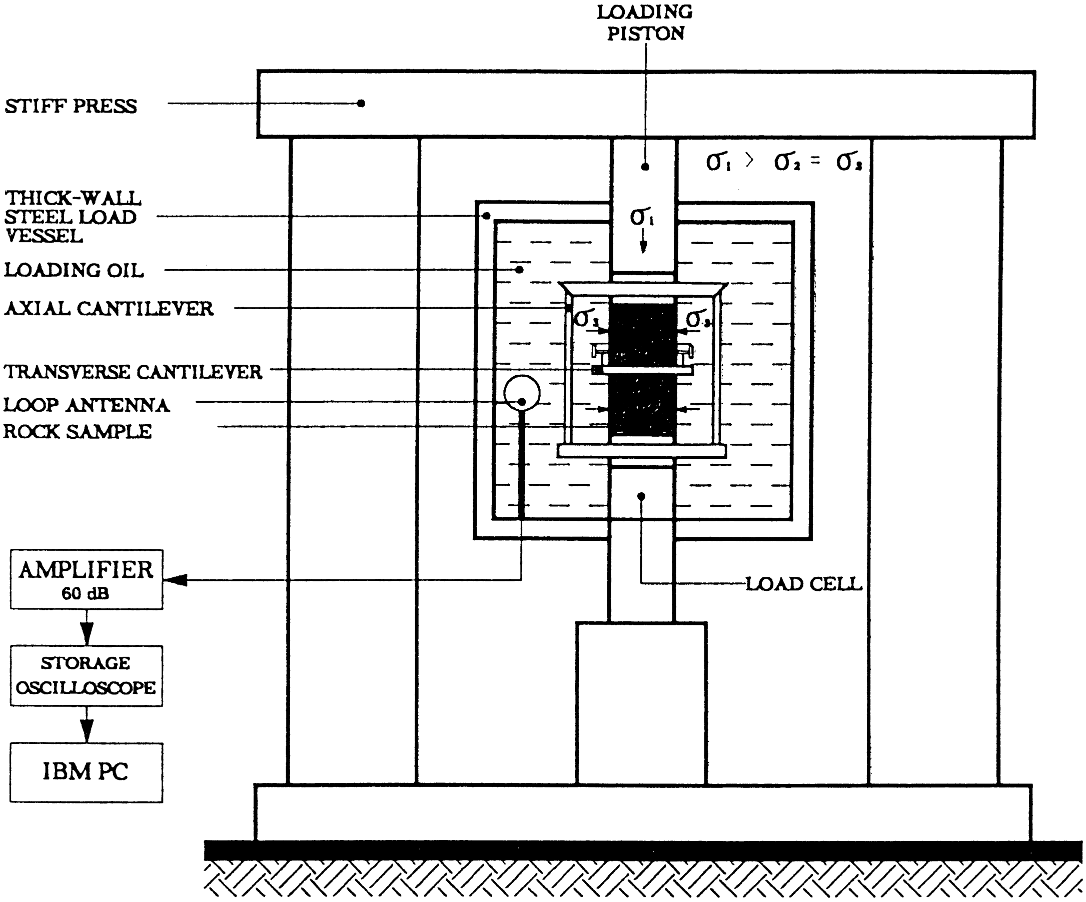

Fig. 4. Schematic diagram of the experimental arrangement.

time during all periods of sample loading. Twenty-four chalk samples were investigated under different loads. Nine samples were loaded uniaxially, while the other fifteen were loaded triaxially.

2.3. Fractographic method

As expected from our previous studies (e.g. Bahat, 1991), the fractured chalk surfaces exhibited an interesting fractography. Following rock failure, the plastic jacket was removed from each sample. The sample was then opened and one of each pair of matching fracture surfaces, larger than 100 mm^2, was traced on a millimeter gridded paper, drawing the boundaries between the tensile and shear zones according to fractographic criteria (see below). The area of each fracture side was manually measured and the sums of all tensile, shear and total areas obtained for each sample were catalogued (Table 1). Area measurement errors were estimated to be up to 10% (mostly along boundaries between tensile and shear areas). The fractography of all the pieces of each sample was then studied using a binocular microscope, both qualitatively and quantitatively.

3. Results

3.1. Fractography

3.1.1. Criteria for the distinction between tensile and shear fracture surfaces

We identified several distinct 'key surface morphologies' (KSM) that belong to the tensile and shear categories. Tensile features include plumes (or striae) and stairs. Shear features include a sugary texture, ridges and grooves (RG) and steps. These KSM and the distinction between stairs and steps are expanded upon below.

Tensile surfaces are planar and relatively smooth with a characteristic matt white-grayish color. Large (25 ± 10 cm^2) tensile surfaces that display uniform factographic features (Fig. 5a) are rare. Most tensile surfaces are divided into domains (Fig. 1c). Sample 7 shows several elongated tensile domains (~5 cm × 2 cm each) that propagated independently and are separated from each other by sharp boundaries (upper center of Fig. 5b). Plumes are characteristically elongated and appear sub-parallel to the cylindrical axis, occasionally deviating (by a few degrees) from this orientation. They initiate independently and have different orientations on surfaces of neighboring

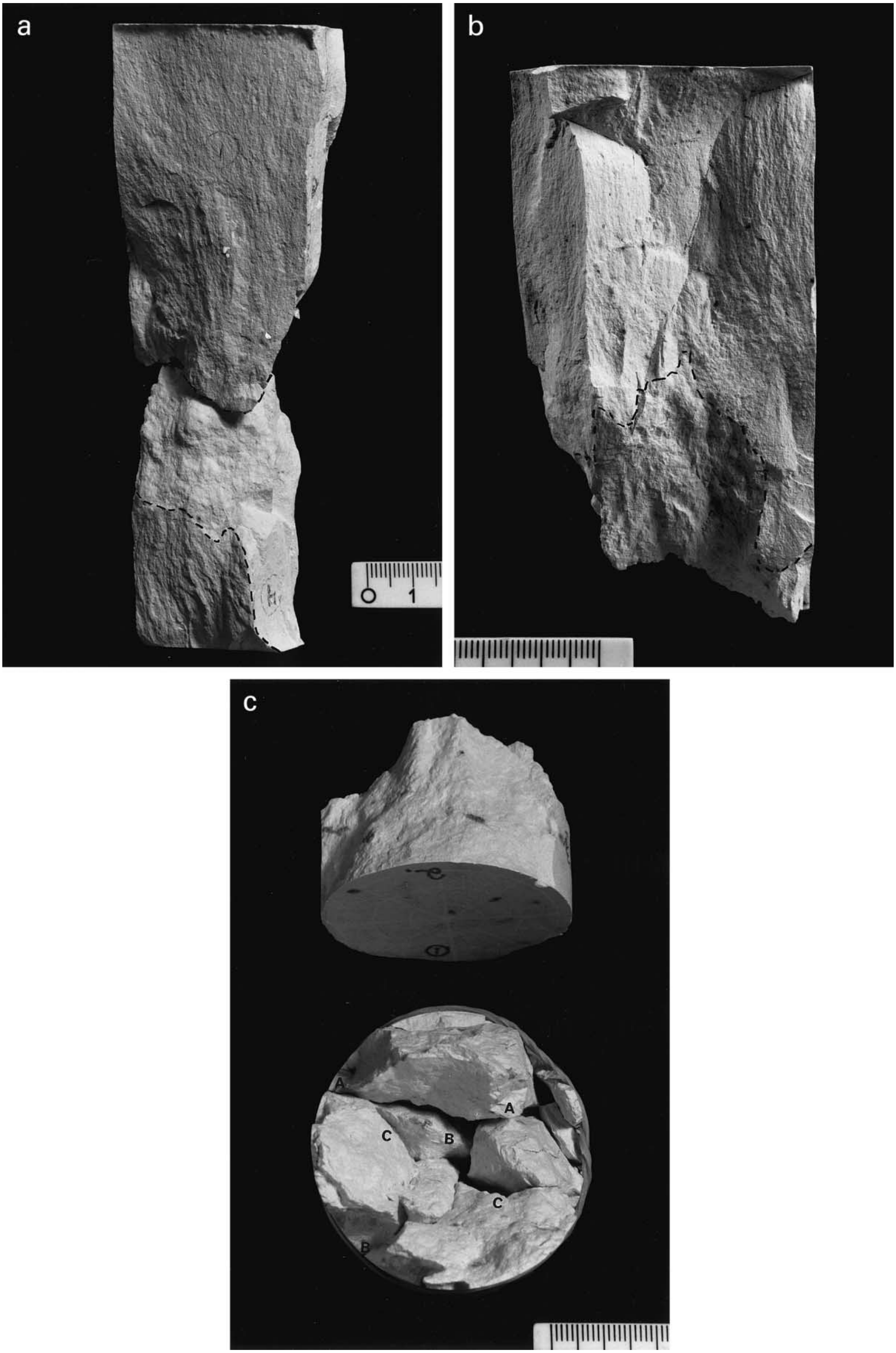
a
0
1
b
c
A
A
C
B
C
B

domains that differ radially in their orientations about the sample axis. A plume consists of many barbs that often appear as a mixture of braids. A barb is an individual stria in the plume that marks the local direction of fracture propagation along a plume (Bahat, 1991, p. 142). Barbs from our tested chalk are fine lines (≤0.5–2 mm in length). Accordingly, some of the plumes are coarse (3 cm in length, while their widths and amplitudes are about 2 mm), whereas others are smaller (width and amplitude are about 0.5 mm or lower). Occasionally micro-undulations (Fig. 2) occur orthogonally to the plumes.

The smooth tensile surfaces may irregularly be disturbed by stairs up to 5 mm in length and 1 mm in height difference that are sub-orthogonal to the direction of plumes (near sample wall, at right side of Fig. 5b). Such stairs result in a division of large surfaces into smaller planar sub-domains at different elevations, ranging in size from 0.5 to 2 cm^2. Sub-domains maintain the general plume orientation within a domain.

The shear sugary texture characterizes peripheries of quasi-conic fractures (Fig. 5c, see Section 3.1.2) and other shear fractures (including those that occur at the circumference of the sample, cutting the cylindrical wall (Fig. 5a). This texture is grainy and white. The sugary fracture is often transformed into a texture of straight ridges and grooves (RG) (1–2 cm long, 2 mm wide and 2 mm amplitude), maintaining the white color and some of the grainy appearance. Occasionally, however, small RG overlap larger ridges (3–4 cm long, 15 mm wide and up to 3 mm amplitude).

A key feature of single shear fractures (Fig. 6a and b) is their strong deviation from planar into concave and convex topographies (Fig. 1b). The surface of the shear meso-fracture (that divides the cylinder into two pieces) is subdivided into adjacent domains (of about 3–10 cm^2 in size) that often vary topographically and exhibit distinct RG, which differ in their intensity and orientation (Fig. 1d). Characteristically, RG deviate no more than 10° from the cylindrical axis. An individual domain on a shear surface is often subdivided into sub-domains (of about 0.5–1 cm^2 in size) that occur at different topographic elevations. RG maintain the same orientation in passing from sub-domain to sub-domain, indicating the continuity of fracture. A sub-domain consists of a set of microcracks (≤0.5–4 mm long) that are aligned along the RG that cross sub-domain boundaries within individual domains.

For shear fractures, the ‘actual’ surfaces have considerably larger areas than the ‘nominal’ ones, while tensile fractures appear to have approximate equality between the ‘actual’ and ‘nominal’ surfaces. Although, superficially, ridges and grooves resemble plumes, they actually differ considerably from each other. The plumes are located on planar tensile surfaces of a grayish color and appear as braids; on the micro-scale the barbs are sub-parallel to the cylindrical axis. The RG are relatively straight and appear parallel to each other within boundaries of individual domains on shear surfaces. RG in neighboring domains may slightly differ in their orientation, such that they often form small angles to the cylindrical axis. Finally, tensile domains show some tendency to have quasi-rectangular boundaries, shear domains have decidedly irregular boundaries.

Steps (1–5 mm long and 0.5 mm wide) are occasionally aligned sub-orthogonal to RG that occur in samples that failed under triaxial conditions and fractured into two pieces (Fig. 6b). In these fractured cylinders, all the steps maintain the same gradient in a given sample such that ‘walking up stairs’ is accomplished along the same direction, as shown by the two matching pieces: towards the respective unfractured ends. This enables us to determine the sense of shear displacement in the fractured sample. Following conventional criteria, it is inferred that the steps were formed during the shear fracture (Twiss and Moores, 1992, Fig. 4.16). The steps in the surface of one piece face in the direction opposite to the motion of the other piece. Hence, steps on shear surfaces differ from stairs on tensile ones by their association with displacement. Often the steps are more pronounced than stairs.

3.1.2. The shapes of quasi-conic fractures and their influence on further fracture

Failure of rock samples often starts at the contact of the circumference of the cylinder with the endcup, where stress concentrations occur. This gives rise to early conic fractures in many compression tests (Jaeger and Cook, 1979, p. 145). In our study, conic fractures were pronounced under both uniaxial and triaxial loading at α values between 18 and 25°. No actual cones were obtained in the chalk under study. Instead, various permutations of this geometry into ‘quasi-cones’ appeared. In some cases, the circular ends of the samples were almost wholly preserved (up to about 300°) (Fig. 5c), in others, only partial cones (of circular ends ≥180°) were formed. Quasi-conic fractures are readily identified by their shear fractographies of combined sugary and RG textures. Occasionally, however, they display tensile fractographies on partly straight fractures that cut the quasi-cones along sub-axial orientation. The critical angle above which tensile fractures transform to shear ones appears to be $\alpha_c = 8 \pm 2°$, close to the 10° observed by Holzhausen and Johnson (1979).

Fig. 5. Photographs of fractured chalks under uniaxial stresses (cm scale). (a) A longitudinal split from sample 8 dominated by an axial tensile fracture. The two tensile parts are displaced in order to show a late inclined shear fracture (between dashed boundaries) that crossed the split. Sub-axial plumes mark the split. (b) A shear fracture that formed by the quasi-cone is transformed into several tensile splits at different radial orientations in sample 7 (dashed line separates shear fracture from a tensile one). Plumes on the split surfaces propagated upwards. (c) Reconstruction of sample 5 to the original cylinder (at upright position, below) and the quasi-cone (axis parallels to picture, above).

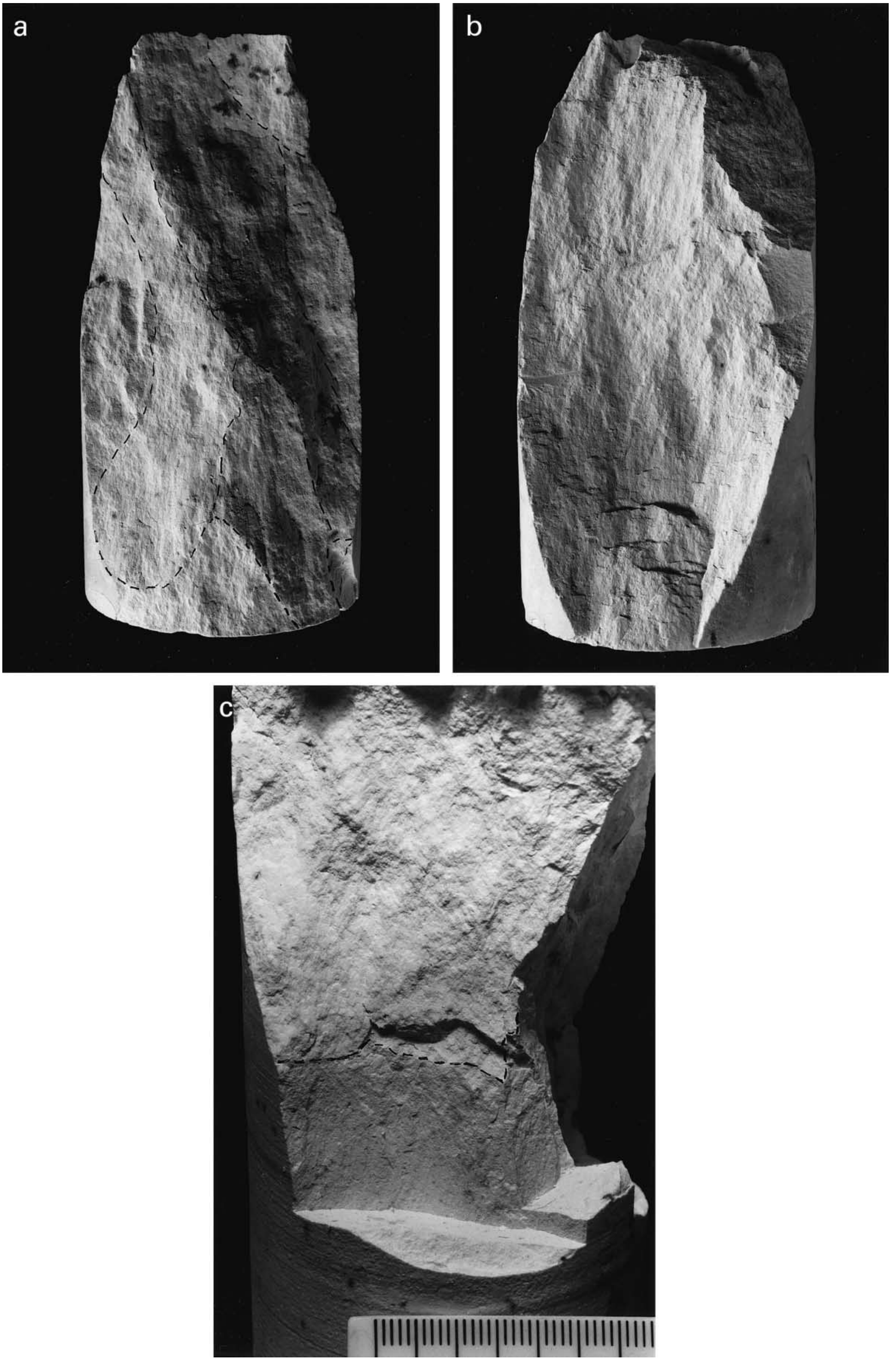
a
b
c

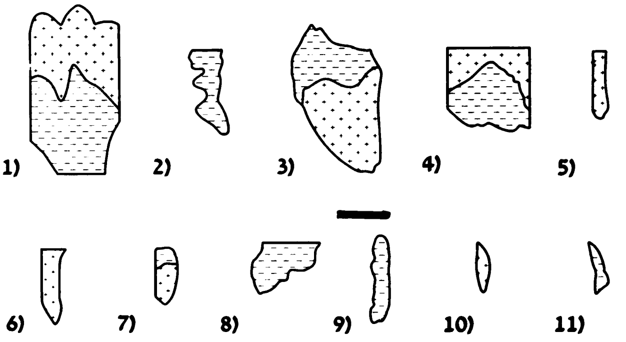

Fig. 7. A display of half of the total number of fracture surfaces (one of each matching couple) from sample 6 in Table 1. Shear surface are marked by − and tensile surface by +. Scale bar is 4 cm.

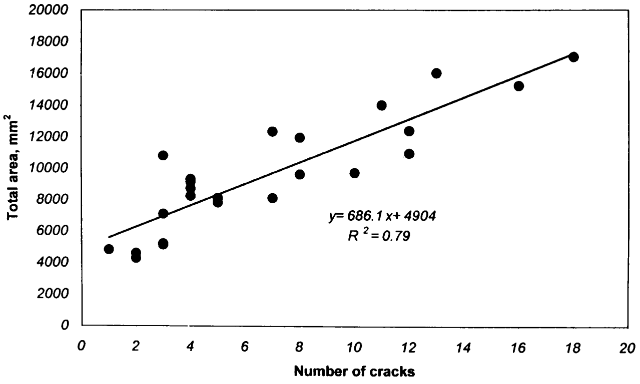

Fig. 8. Relationship between number of fractures (one from each of two matching fractures) and total area of all fractures.

Shear fractures occur on partly curved, inclined surfaces of the quasi-cones. They are commonly followed by large tensile fractures extending from the locations where the cones end (at a distance of some 4–7 cm from the sample end), and cutting the rest of the cylinder (Fig. 1a). There is a greater tendency for longitudinal splits to further subdivide radially into more axial tensile fractures where a more complete circular end was preserved (in the 180–300° range) (Fig. 5c).

3.1.3. Combined failure by shear and tensile fractures

An important part of the fractographic study was the reconstruction of the original cylindrical samples (Fig. 5c). This reconstruction was accomplished mostly by assembling the larger two to five pieces (larger than 4 cm in length). Smaller pieces often constitute a significant volume fraction of the sample. They fill gaps between the large pieces and along the outer wall of the cylinder. A large number of small pieces are visible particularly in samples fractured by uniaxial loading (see below).

With the exception of a few cylinders that fractured either by a single shear fracture or by strongly dominated longitudinal splittings (Fig. 5a), most samples both under triaxial and uniaxial loading, failed by a combination of shear and tensile fracture (Figs. 6c and 7; Table 1). Generally, triaxial failures resulted in a smaller number of fragments (some 1–12 pieces), and in ratios of total shear surfaces to tensile surfaces greater than one. Uniaxial failure, on the other hand, resulted in considerably more fractured surfaces (some 7–18 pieces) and in ratios of total shear surfaces to total tensile surfaces less than one. The total fracture area increases with the number of cracks (and fragments) (Fig. 8). This figure shows that the largest meso-fractues, i.e. single shear fractures (Fig. 1b) have areas of the order of 5600 mm^2. These are considerably larger than the domain fracture size (see Section 3.2.2), while the smaller fractures (Table 1) average ~700 mm^2.

There is a distinct trend of length increase of the longitudinal splits with the decrease of the lateral stresses: from 1 cm (sample 15, $\sigma_3 = 5$ MPa) through 2 cm (sample 25, $\sigma_3 = 2$ MPa) to 4 cm (sample 14, $\sigma_3 = 1$ MPa). This correlation shows that tensile longitudinal splitting also occurs under triaxial stresses, where the extent of the tensile fracture is inversely controlled by the confining pressure. Correspondingly, the ratio of fractured area by shear (SRA)/fractured area by tension (TNA) tends to increase with confining pressure σ_3 (Table 1; Fig. 9).

3.1.4. Failure by single shear fracture

Both similarities and dissimilarities were identified in the fractographies of the three samples that failed by single shear fractures (Nos. 16, 17 and 27). Large deviations from planar fractures into curved surfaces are exhibited by samples 17 and 27 (Figs. 1b and 6a), and small deviations are displayed by sample 16. However, small angular deviations (β) in adjacent domains of the orientation of the RG relative to the cylindrical axis along the dip of the fractures ($\beta = 7$, 12 and 14° for samples 16, 17 and 27, respectively) are common to the three samples. For sample 16, β was uniform, whereas for samples 17 and 27 β had both positive and negative signs at adjacent domains (Fig. 6a and b). That is, for the latter two samples, distinct adjacent domains facing opposite directions occurred at different locations on the curved fracture surfaces.

3.1.5. Relationship and sequence of shear versus tensile fractures

Cross-cutting relationships of fractures that were marked by the key surface morphologies were used as criteria for sequence determination. This determination was facilitated

Fig. 6. Photographs of fractured chalks under triaxial stresses (cm scale). (a) A meso-fracture from sample 27 is divided into distinct domains in which RG slightly change their orientation. Several domains show further divisions into sub-domains. (b) Part of a meso-fracture from sample 17 showing RG and steps. (c) A section of sample 25 shows three parts from bottom to top: the original cylinder, a medium size tensile crack and a large shear crack, respectively.

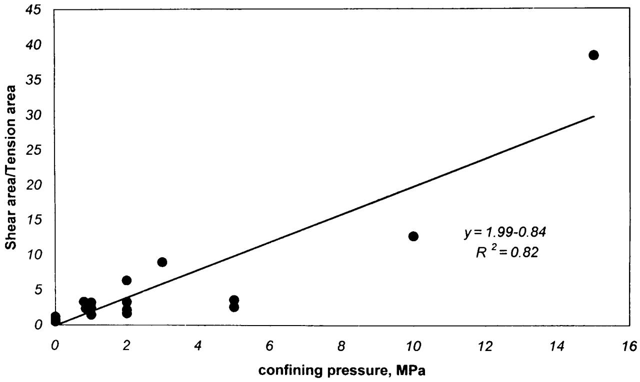

Fig. 9. Relationship between the ratio of fractured area by shear/fractured area by extension, and lateral compression, σ_3.

by the reconstruction of the original cylinders from their pieces (Fig. 5c). Several fracture sequences can be distinguished. Sequence 1. Several stages of longitudinal splitting. Sequence 2. Initiation by quasi-cone and subsequent longitudinal splitting. Sequences 3 and 4. Axial tensile fracture and subsequent inclined shear fracture in two distinct variations. There are, however, samples in which the relative age of shear vs tensile fractures cannot be established.

Sequence 1. Sample 5 exhibits a repeated tensile fracture of the initial longitudinal split. Following the development of a large (anisotropic) longitudinal split (AA in Fig. 5c), a second large, radial fracture (BB) was formed at 65° to the first split. It extended from the first split to the sample wall. The second fracture was then fractured by a third one (CC) that formed 30° with the first split and extended diametrically through the two walls of the cylinder. Additional cracking to smaller pieces occurred subsequently.

Sequence 2. Samples 14 and 7 failed under different loading (triaxial and uniaxial, respectively). Nevertheless, there is a resemblance between their fracture sequences: both exhibit initial quasi-conic shear fractures that ended up in tensile longitudinal splitting. About one half of the sample length is fractured into a quasi-cone fracture and the other half is dominated by a longitudinal splitting in sample 7 (Fig. 5b). Plumes and undulations indicate that the tensile fractures propagated from their areas of contact with the shear fractures (dashed boundary at the upper center part of the sample) towards the other end of the sample, opposite to the one associated with the quasi-cone. At the lower right side of this picture, the convex side of micro-undulations (hardly visible in the picture) faces towards the sample end, also pointing in the same propagation direction.

Sequence 3. Sample 8 exhibits a longitudinal splitting into two major tensile parts along the cylindrical axis (Fig. 5a). In addition, an oblique shear fracture that extends from the wall of the cylinder 6.5 cm from one end cuts the planar surface of the longitudinal split at 2.5 cm from that end. The continuations of the plumes on the planar surfaces from end to end of the sample are clearly seen at both sides of the trace of the shear fracture, showing compellingly the sequence of longitudinal splitting formation before that of the shear fracture.

A second manifestation of sequence 3 is associated with the initial fracture of some quasi-cones. Sub-axial fractures cut the circular ends of samples (for example in sample 20) and exhibit striae (often not longer than 1 to 1.5 cm in length) characteristic of tensile fracture. These early fractures cut the quasi-cones and extend to inclined shear fractures.

Sequence 4. Although this sequence resembles sequence 3, it is classified separately because it relates to a different fracture mechanism. There is a common feature to the fracture of samples 15, 25 and 20 (all failed in triaxial loading). In these samples, tensile fractures that appear at about the middle height of the respective cylinders are transformed (geometrically but not necessarily sequentially) into shear fractures towards one end of the sample. However, these tensile fractures arrest inside their cylinders when propagating in the opposite direction, without reaching the other end (Fig. 6c). This arrest demonstrates that the shear cracks did not control fracture throughout the entire sample length. Apparently, tensile fracture dominated the process along the central parts of the samples. Again, an independent initiation of the two fracture modes is a reasonable possibility. The fracture arrest within the cylinder is quite important (Fig. 6c). It demonstrates the absence of offset between the rock parts separated by the fracture, in contrast to the clear displacements that took place as a consequence of failure in samples 16, 17 and 27 (see steps in Section 3.1.1).

There is a fifth group that needs to be mentioned. Sample 20 predominately failed into four large pieces bounded by shear fractures having surfaces that considerably deviate from planar geometries, and often changing their orientation in all directions. Transient orientations of these fractures include parallelism to the cylindrical axis. At areas of contact, RG differ in their orientation relative to adjacent plumes, and no continuation between these textures can be positively identified. Therefore, no clear sequence could be established between these failure modes. An independent initiation of the different fracture modes cannot be ruled out.

3.1.6. Microcrack populations and their orientations

Our results show that sample failure by single fractures is rare. Most pictures of large fractures are fractographic expressions of composites of fracture domains which consist of microcracks ranging in length from 0.1 mm (limit of measurement) to 4 mm. Microcracks on shear and tensile fractures exhibit different fractographic features. Microcracks on shear fractures are generally elongated parallel to RG, where they maintain their orientation within domain boundaries. As such, their orientation may be tilted by a few degrees (up to about 10°) right or left with respect to the fracture dip (on parallel section) (Fig. 6a and b). Accordingly, they are generally sub-parallel to the fracture dip. The behavior of microcracks on tensile surfaces is shown by the geometry of barbs along plumes. Whereas microcrack lengths can readily be measured between tips on RG, barb lengths on tensile surfaces are not clearly defined, because they are continuously connected along the plumes. However, the general angular behavior of the barbs is similar to that of microcracks on RG, i.e. they are sub-parallel to the fracture dip. Cracks may vary from sub-millimeter to several centimeters in length, where the upper sizes are limited by the sub-domain and domain boundaries. The centimeter-long cracks and the microcracks commonly maintain the same sub-axial orientation.

All the meso-fractures that cut through the chalk cylinders (and have surfaces in the order of 50 cm^2 in size) display fracture-composites of domains and sub-domains consisting of microcrack coalescence. These assemblages are more common on the three-dimensional shear fractures (Fig. 6a), but also occur on planar tensile surfaces. Note, for example, that even the 'uniform' large tensile fracture of sample 8 (Fig. 5a) is divided into a 'lower' surface marked by a delicate plume and an 'upper' surface marked by a coarser one. Both plumes have the same orientations on the two sub-domains, suggesting that the planar fractures propagated in 'sets', much like joint sets in the field.

3.2. Electromagnetic radiation (EMR)

3.2.1. EMR measurements and fracture areas

In previous publications (Rabinovitch et al., 1998, 1999; Frid et al., 1999) it was shown that the parameters derived from the analysis of EMR pulses emanated during fracture can be related to the dimensions of that fracture. Thus, the frequency ω of a pulse is inversely related to the width, b, of the crack by $\omega \sim \pi V_0/b$ where V_0 is the relevant wave velocity (notably the Rayleigh velocity). Also, the crack length ℓ is related to the duration of the interval T' between pulse initiation and the attainment of the maximum of its envelope, $\ell \sim T'V_c$, where V_c is the crack velocity. The area of the crack, S, should therefore be proportional to

$$S \approx \ell b \sim kT'/\omega \tag{2}$$

where k is a proportionality constant, whose dimensions are $\mathrm{mm}^2/\mathrm{s}^2$ (Rabinovitch et al., 2000).

Since a one-to-one correspondence between the EMR pulses and the fractures causing them is not possible in the present measurements, we have concentrated only on the cracks having the largest areas for each experiment (either shear or tensile, Fig. 7) and tried to correlate them with those EMR pulses which showed the largest T'/ω values. Results are shown in Fig. 10 for only 13 samples for which the largest T'/ω values were discernible. As is seen, Eq. (2) provides a very good linear relation between T'/ω values and fracture areas ($R^2 = 0.9$). The ratio of crack area to T'/ω for chalk is therefore $k = 2.52 \times 10^{13}$ $\mathrm{mm}^2/\mathrm{s}^2$, which can henceforth be used to evaluate crack areas, given T'/ω values.

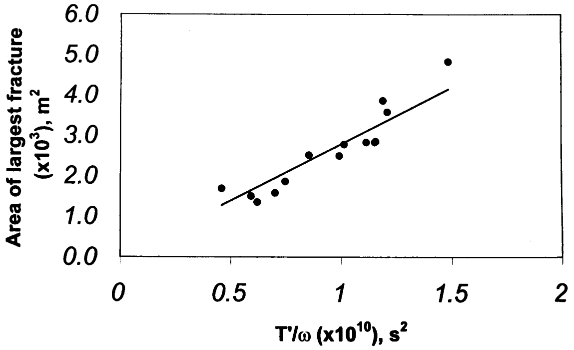

Fig. 10. The relationship between the areas of the largest fracture (either tensile or shear, see Figs. 5, 6 and 7) in each sample and the largest value of T'/ω of the same sample.

3.2.2. The stress-strain vs T'/ω diagrams

The T'/ω points on the diagrams of axial stress vs the axial strain (Fig. 11) represent values for individual EMR pulses that reflect crack dimensions that vary in size through five orders of magnitude. Their appearance sequence is as follows. At stresses below 10 MPa they range from 0.025 to 0.25 mm^2 ($\sim$0.15 mm × 0.15 mm to 0.5 mm × 0.5 mm); then, at stresses between 20 and 30 MPa, they approximately range from 2.5 to 25 mm^2; above 40 MPa, they range from about 250 to about 2500 mm^2.

The detailed results of the four examples (Fig. 11) show distinct fracture paths for both the uniaxial and triaxial tests. There is a 'large jump' in sample 27 between the range 1.E − 15–1.E − 13 to 1.E − 11–1.E − 10 (1.E − 10 is equivalent to 1×10^{-10}) in the approximate strain range 0.003–0.006, whereas a quasi-continuous rate of fracture area growth in the same intervals is exhibited by sample 25. Also, a 'small jump' is shown for sample 8 from 1.E − 11 to 1.E − 10 between the approximate strains 0.005 and 0.007, compared with the quasi-continuous fracture area growth rate in sample 7 through the same intervals.

The large (domain) fracture areas, S of samples 7, 8, 25 and 27, that form close to peak stresses are summarized in Table 2. It is seen that the S values fluctuate in each sample with stress increase, mostly between 500 and 2500 mm^2, with a few exceptions below and above this range. There are, however, considerable deviations in the sums of the S values for each sample. The sum 4277 mm^2 for sample 7 is somewhat lower than the 'nominal' area of 5600 mm^2 (Fig. 8), whereas the sum 7144 mm^2 for sample 8 is above it. For sample 25 this sum, 6292 mm^2, is a little above the nominal, although it was not completely fractured (Fig. 6c). Quite impressive is the large sum 12,897 mm^2 of sample 27. A part of this surplus may be correlated with the strongly curved topography of this sample (Fig. 6a) that significantly adds to the nominal-flat area, but this cannot explain a difference greater than 100%. The explanation of these

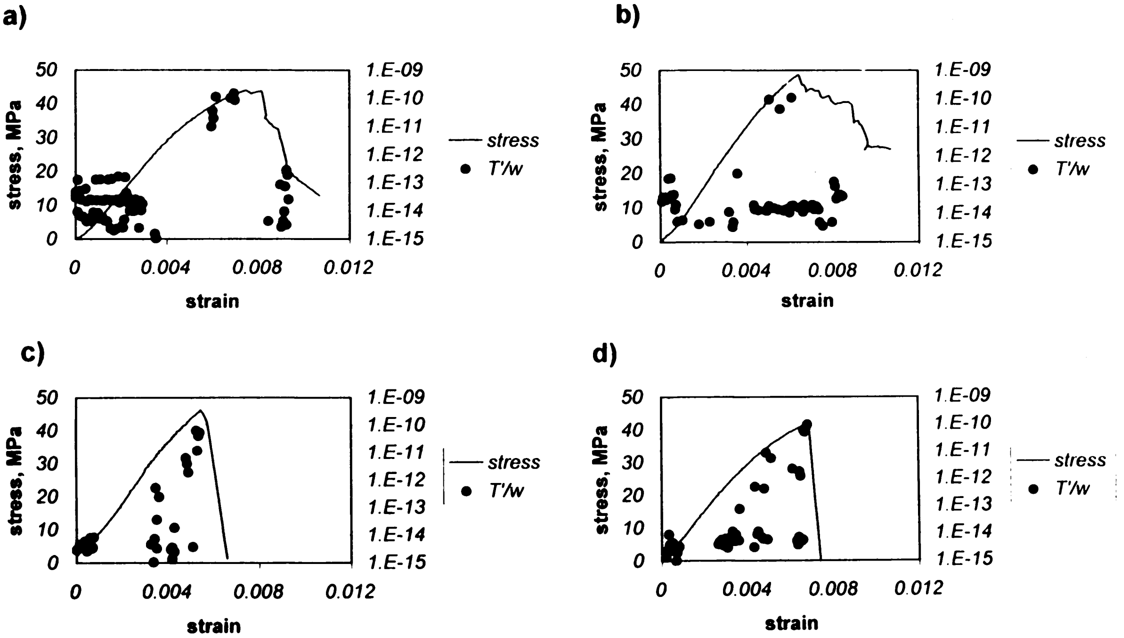

Fig. 11. The spread of T'/ω results that vary across a crack-size scale of five orders of magnitude superposed on the stress versus strain curve. Compared are results for several samples: (a) 27, (b) 25, by triaxial stress, and (c) 7, (d) 8, by uniaxial stress. The notation 1.E − 09 is equivalent to 1×10^{-9}.

discrepancies, particularly the one for sample 27 requires additional studies.

There are good fits between results in Figs. 5, 6 and 11. The seven largest cracks for sample 27 occur close to peak stress (Fig. 11a). This agrees quite well with the fractographic division of the domains on the surface of the meso-fracture (Fig. 6a). Sample 25 was fractured by many microcracks but only three large cracks were recorded by EMR (Fig. 11b). Indeed, only about three domains are discerned fractographically in this sample (Fig. 6c). Sample 7 was also fractured by many cracks but only some seven large ones (Fig. 11c), (two–three shear cracks around the quasi-cone and about five longitudinal splits) actually appear in the sample (Fig. 5b). Sample 8 was fractured into 12 pieces (Table 1) but only into two–three large ones (Figs. 5a and 11d).

In summary, both fractographic and EMR results (Table 2) reveal similar sizes of the largest fractures, mostly ranging from 250 to 2500 mm^2, that form close to peak stresses and these approximately correspond to domains that form in similar ranges by both tensile and shear fracture. Discrepancies between calculated and nominal sums of

Table 2
Summary of calculated (according to Eq. (2)) surface areas of the largest individual domains for four samples

Sample number	Axial strain ($\times 10^{-3}$)	Stress (MPa)	$T'/\omega \times 10^{-11}$ (s^2)	S (crack area, mm^2)
7	5.246	44.98	6.34	1585
	5.297	45.27	1.19	297
	5.348	45.57	4.12	1030
	5.398	45.71	5.46	1365
8	6.611	41.3	6.20	1550
	6.658	41.35	5.35	1337
	6.706	41.54	7.12	1780
	6.800	41.75	9.91	2477
25	5.071	41.37	9.64	2410
	5.567	44.33	4.43	1107
	6.113	47.34	11.1	2775
27	5.953	39.25	0.99	247
	6.002	39.51	3.62	905
	6.051	39.73	1.94	485
	6.150	40.15	11.3	2825
	6.790	42.23	10.3	2575
	6.937	42.73	14.9	3725
	6.986	42.78	8.54	2135

fractured areas for individual samples need further investigation.

4. Discussion

4.1. Comparison of results obtained on weak rocks

There is a strong resemblance between fracture features observed in the present study and those obtained in studies on gypsum (Shen et al., 1995; Bobet and Einstein, 1998). The fracture patterns obtained in the 'pristine' (non prefractured) chalk cylinders generally matched well with the fracture patterns obtained in the prismatic specimens of gypsum (Fig. 12a and b). Apparently, the quasi-cones in the chalk samples played an equivalent role to that of the inclined flaws in the gypsum in inducing initial shear fractures in the samples. Particularly important in all these experiments is the orientation of the newly formed cracks relative to the axial compression: they are tensile when parallel/sub-parallel to the axis, and assume shear characteristics as the cracks reach a critical inclination, $\alpha_c = 8 \pm 2°$ to the axis. These orientations also determine the style of transition between shear and tensile cracks. When shear and tensile cracks coalesce and extend, they maintain the same rule; tensile ones have the tendency to be parallel to σ_1 and the shear cracks are inclined.

Two differences from results obtained for gypsum need be mentioned. Firstly, some fractures maintain their shear fractographies in the chalk even along transient sub-axial orientation (as mentioned in Section 3.1.5). These cases probably reflect crack inertia effects under conditions of rapid propagation. Secondly, wing cracks in gypsum initiate from the tips of the inclined flaws and have to curve before assuming axial orientation. In contrast, tensile fractures in chalk are straight. The tensile fractures, either: (a) continue inclined shear fractures, (b) are induced in tension by other stress concentrators, mainly by the contact of the cylinders with the endcups (creating sub-axial fractures that cut the quasi-cones), or (c) they start in the middle of the cylinders where there is no influence of the quasi-cones (Section 3.1.5). The latter tensile fractures are generally planar, straight and much larger than wing cracks.

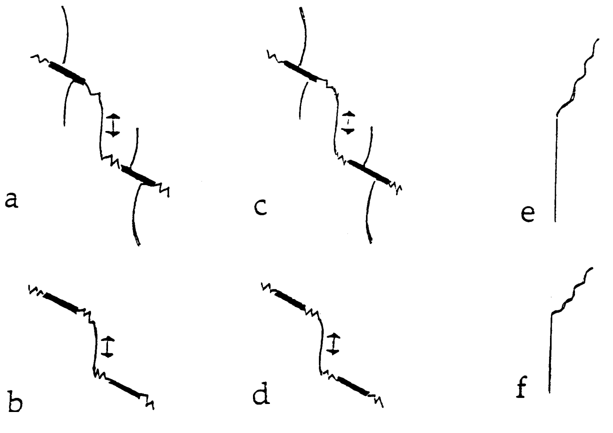

Fig. 12. Schematic summaries of six modes of crack propagation from two experiments on weak rocks, (a and b) in uniaxial compression, and (c and d) in biaxial compression. Thick inclined lines are preexisting flaws, zig-zag inclined lines are new shear fractures and sub-vertical, slightly curved thin lines are wing cracks (from Bobet and Einstein, 1998, Tables 3 and 4). (e) in uniaxial compression, and (f) in triaxial compression from present study (without preexisting flaws): shear fractures show ragged profiles and are inclined, and tensile fractures are straight and parallel to σ_1, not showing wing curvature.

4.2. Experimental fracture surfaces vs natural ones

So far, fractography of failure dominated by (tensile) mode I, has been primarily represented by three typical fracture morphologies on joint surfaces: undulations, plumes and en échelon fringes (Fig. 2). These are also identified on mode I, experimentally-induced chalk fracture surfaces, while plumes (striae) are the most dominant morphology (Fig. 5). Hence, fractographic features that range in size from tens of centimeters to tens of meters in natural exposures may be scaled down experimentally to the centimeter to sub-millimeter scales. Stairs have been identified in experimental samples (Fig. 5b) but have not really been investigated in geological outcrops. Perhaps more attention should be paid in future studies to the role of stairs on joint surfaces.

Fault surfaces, often contain 'slickenside lineations' parallel to the direction of the last slip caused by a mode II (shear) operation, and associated steps. These features appear in many rocks in a 'ridges and grooves' style, resembling the RG and steps experimentally induced in chalk in much smaller dimensions (Fig. 6). The resemblance of the RG and steps among the different scales implies that the experiment constitutes an adequate simulation of these morphologies in nature. Quite intriguing, however, is the rarity of slickenside lineations on fault surfaces cutting chalks in Israel. Perhaps the strong friction involved in faulting prevented the 'survival' of slickensides in the soft chalks.

4.3. The smallest microcracks

The large EMR pulse populations at low stresses are obtained from many microcracks. Some of these microcracks possibly reflect dilatancy under both uniaxial and triaxial loadings. Dilatancy is generally understood to occur between one- and two-thirds of the macroscopic fracture stress and is associated with an opening normal to σ_1 of microcracks throughout the sample (Brace et al., 1966). In contrast, our EMR results repeatedly show pulses representing microcracks that started to form much earlier than one-third of the peak stress (Fig. 11). Sprunt and Brace (1974) observed that stress-induced microcracks are distinguishable from the initial defects in the rock in their shapes and orientations. The stress-induced microcracks are sharp-ended and elongated sub-parallel to σ_1, whereas the initial defects are blunt and are oriented in all directions. Our results show that EMR pulses can be correlated with microcracking throughout most of the stress range. This includes pulses at the lower range of σ_1, probably in association with the deformation of 'initial defects' (pores?). Note that since EMR pulses are created solely by cracks and not by existing defects, this deformation must consist of some cracking.

4.4. Ridges and grooves and incipient shear before failure

Ridges and grooves (RG) are elongated lineations (slickenlines/slickensides) parallel to the direction of relative slip on fault surfaces. However, their origin is not clear (Davis and Reynolds, 1996, p. 277). It is not understood why continuous lineations are longer than the known displacement along faults (Hobbs et al., 1976, p. 303) and how these lineations can be formed when the displacement is negligible (Means, 1987). Our results only exacerbate this dilemma. We obtained RG on fractured surfaces that had practically zero displacement. These surfaces (e.g. samples 15 and 25) did not cut through their respective cylinders; instead, they were arrested within the samples (Fig. 6c). The close resemblance of the RG in the latter samples to RG that occur on surfaces that were relatively displaced (e.g. sample 16) is also intriguing: the only fractographic difference is that steps occur on the fracture surface of sample 16 but not on that of sample 15. The implication is that RG develop by the shear process during a decrease in sample cohesion due to microcracking prior to failure. The clear morphology of the plumes in these cases is a compelling indication of the lack of relative displacement on them, because such displacements would have erased the delicate plumes.

We can therefore distinguish between an incipient shear when some, but not total, cohesion is lost. This is the time when the grooves and ridges are formed. A later displacement is recorded by steps that can be assigned to a total loss of cohesion. These observations resemble results obtained by Wibberley et al. (2000) who identified an 'incipient breakdown zone' at the immediate tip of the microfault. This zone consisted of early, long, pervasive tensile microcracks, oriented parallel to σ_1 that were later cross-linked by a set of perpendicular short tensile microcracks, leading to a subsequent failure.

4.5. Inclined shear and axial tensile meso-fractures

The strong correlation between crack orientation and mode of propagation (Section 4.1) relates to mini-fractures (several millimeters to several centimeters in length) and to meso-fractures (up to about 10 cm in length). This correlation does not automatically apply to microcracks below 0.1 mm in size, for which we do not have accurate fractographic observations.

If, however, this correlation could be confirmed for micro-sized cracks, it might have important implications regarding the transition from microcracks to meso-fractures close to the triaxial peak stresses. This would imply that the axial tensile microcracks were connected by oblique shear microcracks. It would correspond to the observations by Shen et al. (1995) and Bobet and Einstein (1998) on fractures in gypsum, and by us on inclined shear fractures in chalks. This scenario would also coincide with the micromechanism of crack interaction at the tip of a propagating microfault (Wibberley et al., 2000). Note that Hoek and Bieniawski (1966) also suggest that early microcracks are linked by inclined shear cracks, with the difference that these authors assumed the early microcracks to be inclined to σ_1. The 'connection' by oblique shear microcracks would differ, however, from the models by Horii and Nemat-Nasser (1985) and Reches and Lockner (1994), who advocate that such a connection is carried out in granite by tensile microcracks. Additional experiments backed up by close fractographic examination of induced tensile/shear fractures should help to ascertain whether the application of results on microcrack linkage obtained on weak materials (gypsum and chalk) to strong ones (e.g. granite) is justified.

4.6. Earthquake modeling

Rupture associated with earthquakes is apparently analogous to fracture within an intact rock sample subjected to triaxial loading (Reches, 1999). Some previous investigations were related to the understanding of the mechanisms of slip nucleation of earthquakes via the development of a 'process zone' through the interaction of early cracks. This interaction leads to unstable slip and failure of the rock along a fault that forms at about 30° with σ_1. Models of earthquake mechanisms, seismic data and carefully drafted maps of the rupture patterns a short time following an earthquake were compared with results of fracture simulation of various materials (e.g. granite by Reches and Lockner (1994) and Reches (1999) under triaxial loading). However, in contrast to the narrow process zones and faults obtained in the laboratory and shown in earthquake models, actual rupture maps often occur as belts of shear zones of multi-fractures that are 50–200 m wide (e.g. Fig. 13). These belts include both left and right-lateral shears, major and minor tensile fractures, local thrusts and grabens with many bifurcating faults and secondary en échelon fractures (e.g. Allen et al., 1968; Bahat, 1982; Johnson et al., 1994a,b; Reches, 1999). Johnson et al. (1994b) also pointed out the similarities in structural complexities among the Landers 1992 earthquake (Fig. 13) and several earlier ones.

There are, indeed, long stretches of narrow and straight faults along the San Andreas fault system. It may also be theorized that underneath the wide belts of surface rupture, most of the slip concentrates along a narrow zone (Chester et al., 1993). Therefore, is it possible that failure by both single shear and multi-fractures that occur in triaxial experiments, should correspond to 'narrow' and 'wide' types of earthquake rupture, respectively?

Our results, which exhibit failure by multi-fractures, differ significantly from fracture models that advocate a crack evolution into a single oblique process zone (Reches

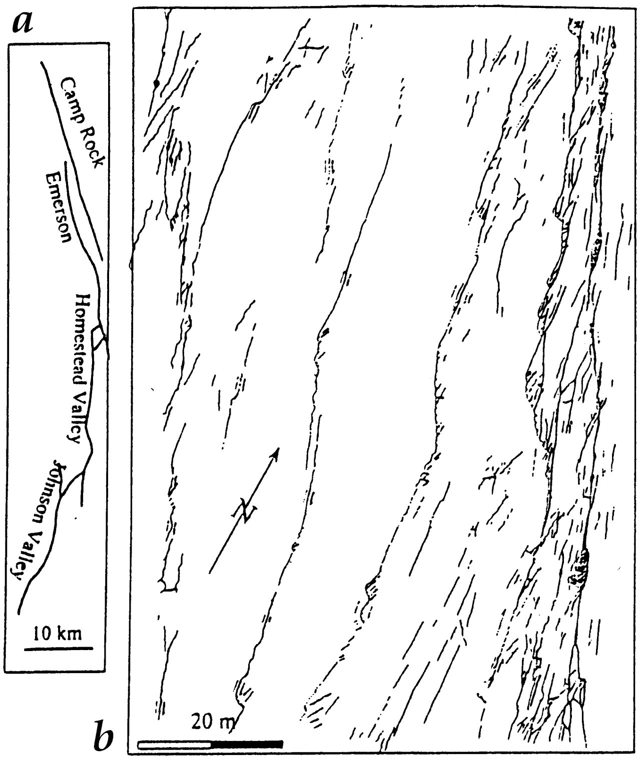

Fig. 13. Features of surface rupture associated with the 1992, magnitude 7.5 Landers earthquake along part of the Homestead Valley segment, California. (a) Generalized map. (b) Detailed map, showing the rupture zone that exhibits various structural elements across a belt of shear zones that is 50–200 m wide (modified after Johnson et al. (1994a) and Reches (1999)).

and Lockner, 1994). It is quite feasible that our results characterize chalks that are weak rocks, and do not characterize strong rocks like granite. In weak rocks, instead of intense crack interaction leading to a single process zone, individual domains grow independently. This would explain why there are many small and medium sized fractures in samples that failed under triaxial compression conditions. It is also possible that the large porosity of chalks hinders crack interaction that could lead to the development of the damage zones that were observed in granite. The multi-fracture complexes exhibited by the chalk samples have greater resemblance to surface ruptures that display wide belts of shear zones associated with some earthquakes (Johnson et al., 1994a) than the single slip surfaces simulated by experiments (e.g. Hallbauer et al., 1973; Reches, 1999). The possible implication is that fracture in weak crusts is better simulated on weak rocks than on strong ones.

5. Conclusions

5.1. Fracture and fractography

The drying and desiccation procedures of the chalk resulted in high strength results ($\sigma_1 - \sigma_3$) which ranged from 37.7 to 52.6 MPa.

We identified several 'key surface morphologies' according to tensile and shear categories. Tensile features include plumes (or striae) and stairs. Shear features include a sugary texture, ridges and grooves (RG) and steps.

The plumes appear as braids on planar tensile surfaces of a matt white-grayish color and on the micro-scale the barbs are sub-parallel to the cylindrical axis.

The RG appear on sheared white sugary, ragged surfaces that form curved topographies within boundaries of individual domains. RG in neighboring domains may form small angles with the cylindrical axis.

Domains of all tensile surfaces are planar and smooth, either parallel or sub-parallel to the cylindrical axis.

Domains of shear surfaces consist of microcracks ranging from 0.1 to 4 mm in length that are associated with RG, which are either parallel or sub-parallel to the fracture dip. No wing cracks were found on the fracture surfaces.

Whereas (tensile) longitudinal splitting can stretch continuously on a parallel plane or on adjacent parallel planes, shear failure into meso-fractures combines a series of distinct domains on separate surfaces that slightly differ in curvature and orientation.

Surfaces of shear fractures have considerably larger areas than the 'nominal' ones, whereas in tensile fractures 'actual' and 'nominal' surfaces are comparable.

We distinguish four fracture sequences: 1. Several stages of longitudinal splitting (LS). 2. Initial quasi-cone and subsequent LS. 3. LS that initiated from around the sample end, and subsequent inclined shear fracture, and 4. LS that initiated from around the sample center, and subsequent inclined shear fracture.

Conic and incomplete 'quasi-cones' may be obtained under both uniaxial and triaxial tests.

The patterns of the tensile fractures often vary with the shape of the quasi-cones from two large matching longitudinal splits to repeated subdivisions into radial LS.

Triaxial failures resulted in a few fractures and in ratios of total shear to tensile surfaces >1, while uniaxial failure resulted in many fractures and in ratios of total shear to tensile surfaces <1.

Most large fractures are composites of fracture domains.

Generally, the sequence on shear surfaces is: incipient shear fracture displayed by RG before total loss of cohesion, followed by displacement shown by steps.

Fractures by both uniaxial and triaxial compression show that there is a strong correlation between the orientation of cracks and their mode of propagation: shear cracks are inclined to σ_1 while tensile cracks are parallel or sub-parallel to σ_1. The transitional angle between the two is $\alpha_c = 8 \pm 2°$.

This correlation possibly supports previous suggestions that early microcracks are linked by inclined shear cracks (e.g. Hoek and Bieniawski, 1966), rather than by tensile cracks.

5.2. Electromagnetic radiation

We correlated throughout the stress range variations of the EMR pulse parameter T'/ω to changes of crack sizes in the fractured chalk, where T' is the time from the pulse origin to the maximum of its envelope and ω is the pulse frequency.

A linear relation between the areas of the largest fractures of each sample and the largest T'/ω values was established, yielding a general such relation $S = kT'/\omega$, where k was found to be 2.52×10^{-13} mm^2/s^2. This relation enables us to correlate crack areas from the smallest ($\sim$0.01 mm^2) to the largest ones ($\sim$2500 mm^2) with their appearance times along the stress-strain process. The ranges of the largest cracks (domains by both tensile and shear fracture) fit well this upper range.

5.3. Application to earthquake modeling

The multi-fracture complexes exhibited by the chalk samples bear a greater resemblance to surface ruptures that display wide belts of shear zones (associated with earthquakes that occurred in weak crusts), than to single slip surfaces simulated in strong rocks. The possible implication is that fracture in weak crusts is better simulated on weak rocks than on strong ones.

Acknowledgements

We would like to thank the Israel Science Foundation founded by the Israel Academy of Sciences and Humanities, the Earth Sciences Administration of the Ministry of Energy and Infrastructure, and Izvonot Committee of Israeli Government Estate Distributions for supporting our research. We are grateful for technical help from V. Palchik and M. Brima. We would like to thank Peter Bankwitz, John Cole and C.W. Passchier for very useful comments on an earlier version that helped to considerably improve the paper.

References

Allen, C.R., Castle, R.O., Clark, M.M., Grantz, A., Sharp, R.V., Theodore, T.G., Wolfe, E.W., Young, T.L., Geology students from CALTECH, 1972. Map showing surface ruptures created at the time of and after the Borrego Mountain Earthquake of April 9, 1968 (GMT) US Geological Survey, Professional Paper 787, Plate 1.

Bahat, D., 1982. Extensional aspects of earthquake induced ruptures determined by an analysis of fracture bifurcation. Tectonophysics 83, 163–183.

Bahat, D., 1991. Tectonofractography. Springer-Verlag, Heidelberg 354pp.

Bahat, D., Grossenbacher, K., Karasaki, K., 1999. Mechanism of exfoliation joint formation in granitic rocks at Yosemite National Park. Journal of Structural Geology 21, 85–96.

Bella, F., Bjadji, P.F., Della Monica, J., Zilpimiani. D.O., Mandzfaladzhe, P.V., Pokhotelov. O.A., 1992. Observation of natural electromagnetic radiation during earthquake in central Italy. Physics of the Solid Earth 28, 88–94.

Bobet, A., 2000. The initiation of secondary cracks in compression. Engineering fracture mechanics 66, 187–219.

Bobet, A., Einstein, H.H., 1998. Fracture coalescence in rock-type materials under uniaxial and biaxial compression. International Journal of Rock Mechanics, Mining Sciences and Geomechanics Abstracts 35, 863–888.

Brace, W.F., Paulding, J.B.W., Scholz, C., 1966. Dilatancy in the fractureof crystalline rocks. Journal of Geophysical Research 71, 939–953.

Burland, J.B., 1990. Preface. In: Burland, J.B. (Ed.). Chalk. Proceedings of the International Chalk Symposium, Brighton, UK, pp. 1–4.

Chester, F.M., Evans, J.P., Biegel, R.L., 1993. Internal structure and weakening mechanisms of the San Andreas Fault. Journal of Geophysical Research 98, 771–786.

Cress, G.O., Brady, B.T., Rowell, G.A., 1987. Sources of electromagnetiuc radiation from fracture of rock samples in the laboratory. Geophysical Research Letters 14, 331–334.

Davis, G.H., Reynolds, S.J., 1996. Structural Geology of Rocks and Regions. John Wiley & Sons, New York 776pp.

Fifolt, D.A., Petrenko, V.F., Schulson, E.M., 1993. Preliminary study of electromagnetic emissions from cracks in ice. Philosophical Magazine B 67 (3), 289–299.

Frid, V., 1997a. Electromagnetic radiation method for rock and gas outburst forecast. Journal of Applied Geophysics. 38, 97–104.

Frid, V., 1997b. Rock-burst hazard forecast by electromagnetic radiation excited by rock fracture. Journal of Rock Mechanics and Rock Engineering 30, 229–236.

Frid, V., Rabinovitch, A., Bahat, D., 1999. Electromagnetic radiation associated with induced triaxial fracture in granite. Philosophical Magazine Letters 79, 79–86.

Frid, V., Bahat, D., Goldbaum, J., Rabinovitch, A., 2000. Experimental and theoretical investigations of Electromagnetic radiation induced by rock fracture. Israel Journal of Earth Sciences 49, 9–19.

Ghosh, S.K., 1993. Structural Geology. Pergamon Press, Oxford, 598pp.

Griggs, D.T., Handin, J., 1960. Observations on fracture and hypothesis of earthquakes. In: Griggs, D.T., Handin, J. (Eds.). Rock Deformation. Memoir of the Geological Society of America 79, pp. 347–364.

Hallbauer, D.K., Wagner, H., Cook, N.G.W., 1973. Some observations concerning the microscopic and mechanical behaviour of quartzite in stiff triaxial compression tests. International Journal of Rock Mechanics, Mining Sciences and Geomechanics Abstracts 10, 713–726.

Hobbs, B.E., Means, W.D., Williams, P.F., 1976. An Outline of Structured Geology. John Wiley & Sons, New York, 571pp.

Hoek, E., Bieniawski, Z.T., 1966. Fracture propagation mechanism in hard rock. Proc. First Congress of International Society of Rock Mechanics, Lisbon 1, 243–249.

Holzhausen, G.R., Johnson, A.M., 1979. Analyses of longitudinal splitting of uniaxially compressed rock cylinders. International Journal of Rock Mechanics and Mining Sciences and Geomechanics Abstracts 16, 163–177.

Horii, H., Nemat-Nasser, S., 1985. Compression induced microcrack growth in brittle solids: axial splitting and shear failure. Journal of Geophysical Research 90, 3105–3125.

Jaeger, J.C., Cook, N.G.W., 1979. Fundamentals of Rock Mechanics. Chapman and Hall, London, 593pp.

Jagasivamani, V., Iyer, K.J.L., 1988. Electromagnetic emission during fracture of heat-treated spring steel. Materials Letters 6, 418–422.

Johnson, A.M., Fleming, R.W., Cruikshank, K.M., 1994a. Shear zones formed along long, straight traces of fault zones during the 28 June 1992 Landers California, earthquake. Bulletin of the Seismological Society of America 84, 499–510.

Johnson, A.M., Cruikshank, K.M., Fleming, R.W., 1994. Borrego Mountain, Loma Prieta, Landers, Northridge; simply earthquakes or seismostructural events? EOS 75 (Suppl. 343).

Khatiashvili, N., 1984. The electromagnetic effect accompanying the fracturing of alkaline halide crystals and rocks. Physics of the Solid Earth 20, 656–661.

King, C.Y., 1983. Electromagnetic emission before earthquake. Nature 301, 377.

Means, W.D., 1987. A newly recognized type of slickenside striation. Journal of Structural Geology 9, 585–590.

Mogi, K., 1985. Earthquake Prediction. Academic Press, Tokyo, 382pp.

Nemat-Nasser, S., Horii, H., 1982. Compression-induced nonplanar crack extension with application to splitting, exfoliation, and rockburst. Journal of Geophysical Research 87, 6805–6821.

Nesbitt, A.C., Austin, B.A., 1988. The emission and propagation of electromagnetic energy from stressed quartzite rock underground. The Transactions of the South African Institute of Electrical Engineers 79, 53–56.

Nettel, S., 1995. Wave Physics. 2nd ed. Springer Verlag, Berlin, 252pp.

Nitsan, V., 1977. Electromagnetic emission accompanying fracture of quartz-bearing rocks. Geophysical Research Letters 4, 333–336.

O'Keefe, S.G., Thiel, D.V., 1995. A mechanism for the production of electromagnetic radiation during fracture of brittle materials. Physics of the Earth and Planetary Interior 89, 127–135.

Ogawa, T., Oike, K., Miura, T., 1985. Electromagnetic radiation from rocks. Journal of Geophysical Research 90, 6245–6249.

Rabinovitch, A., Bahat, D., Frid, V., 1996. Emission of electromagnetic radiation by rock fracturing. Zeitschrift für Geologische Wissenschaften 24, 361–368.

Rabinovitch, A., Frid, V., Bahat, D., 1998. Parametrization of electromagnetic radiation pulses obtained by triaxial fracture in granite samples. Philosophical Magazine Letters 77, 289–293.

Rabinovitch, A., Frid, V., Bahat, D., 1999. A note on the amplitude-frequency relation of electromagnetic radiation pulses induced by material failure. Philosophical Magazine Letters 79, 195–200.

Rabinovitch, A., Frid, V., Bahat, D., Goldbaum, J., 2000. Fracture area calculation from electromagnetic radiation and its use in chalk failure analysis. International Journal of Rock Mechanics & Mining Sciences and Geomechanics Abstracts 37, 1149–1154.

Reches, Z., 1999. Mechanisms of slip nucleation during earthquakes. Earth and Planetary Science Letters 170, 475–486.

Reches, Z., Lockner, D.A., 1994. Nucleation and growth of faults in brittle rocks. Journal of Geophysical Research 99, 18159–18173.

Scott, T.E., Nielsen, K.C., 1991. The effects of porosity on the brittle-ductile transition in sandstones. Journal of Geophysical Research 96, 405–414.

Shen, B., Stephensson, O., Einstein, H.H., Ghahreman, B., 1995. Coalescence of fractures under shear stresses in experiments. Journal of Geophysical Research 100, 5975–5990.

Sprunt, E.S., Brace, W.F., 1974. Direct observations of microcavities in crystalline rocks. International Journal of Rock Mechanics and Mining Sciences and Geomechanics Abstracts 11, 139–150.

Twiss, R.J., Moores, E.M., 1992. Structural Geology. Freeman & Company, New York, 532pp.

Urusovskaja, A.A., 1969. Electric defects associated with plastic deformation of ionic crystals. Soviet Physics. Uspekhi 11, 631–643.

Warwick, J.W., Stoker, C., Meyer, T.R., 1982. Radio emission associated with rock failure: possible application to the great Chilean earthquake of May 22, 1960. Journal of Geophysical Research 87, 2851–2859.

Wibberley, C.A.J., Petit, J.-P., Rives, T., 2000. Micromechanics of shear rupture and the control of normal stress. Journal of Structural Geology 22, 411–427.

Yamada, I., Masuda, K., Mizutani, H., 1989. Electromagnetic and acoustic emission associated with rock fracture. Physics of the Earth and Planetary Interior 57, 157–168.

Yoshino, T., Tomizawa, I., 1989. Observation of low-frequency electromagnetic emissions as precursors to volcanic eruption at Mt. Mihara during November, 1986. Physics of the Earth and Planetary Interior 57, 32–39.